0794

The Effect of Oblique Image Slices on the Accuracy of Quantitative Susceptibility Mapping and a Robust Tilt Correction Method

Oliver C. Kiersnowski[1], Anita Karsa[1], John S. Thornton[2], and Karin Shmueli[1]
[1]Department of Medical Physics and Biomedical Engineering, University College London, London, United Kingdom, [2]UCL Queens Square Institute of Neurology, London, United Kingdom

Synopsis

Quantitative susceptibility mapping (QSM) using the MRI phase to calculate tissue magnetic susceptibility is finding increasing clinical applications. Oblique image slices are often acquired to facilitate radiological viewing and reduce artifacts. Here, we show that artifacts and errors arise in susceptibility maps if oblique acquisition is not properly taken into account in QSM. We performed a comprehensive analysis of the effects of oblique acquisition on brain susceptibility maps and compared tilt correction schemes for three susceptibility calculation methods, using a numerical phantom and human in-vivo images. We demonstrate a robust tilt correction method for accurate QSM with oblique acquisition.

Introduction

Quantitative susceptibility mapping (QSM) is finding increasing clinical applications. Acquisition of oblique image slices is common clinical practice to facilitate radiological viewing but pilot studies suggest this gives incorrect susceptibility (χ) estimates when unaccounted for[1]. Using a numerical brain phantom[2], we performed a comprehensive analysis of the effects of oblique acquisition and compared proposed tilt correction methods for the final χ calculation step in the QSM pipeline. We confirmed these results *in vivo*, and demonstrate a robust tilt correction method for accurate χ calculation.

Methods

Numerical Phantom:

Local field maps were obtained from a non-linear fit[3] over echo times of complex data, created from magnitude and phase images of a numerical brain phantom[2], with no background fields. These background-field-free maps were used to independently analyse the χ calculation step in the QSM pipeline without confounds from phase unwrapping or background field removal. To simulate oblique slice acquisition, the untilted reference local field map (at 0°) was tilted by -45° to +45° in 5° steps. All rotations were carried out about the *x*-axis (*u*-axis, Figure 1) using FSL FLIRT[4] with trilinear interpolation.

We tested four proposed tilt correction schemes (Figure 1):

- *RotPrior*: image rotated into scanner frame prior to χ calculation (with a *k*-space dipole defined in the scanner frame)
- *DipK*: image left unaligned (*k*-space dipole defined in the tilted image frame)
- *DipIm*: image left unaligned (image-space dipole defined in the tilted image frame)
- *NoRot*: image left unaligned (simulating mistaken definition of the *k*-space dipole in the scanner frame misaligned to the tilted image)

To facilitate comparisons, all susceptibility maps left in the image-frame after correction (*DipK*, *DipIm* and *NoRot*) were rotated back into alignment with the scanner axes. These schemes were compared for three χ calculation methods: thresholded *k*-space division (TKD)[5] (threshold = 2/3), iterative fitting with Tikhonov regularisation[6,7] ($\alpha = 0.003$), both corrected for χ underestimation[8], and weighted linear total variation (wlTV) regularisation (FANSI toolbox[9,10], $\alpha = 2\times10^{-4}$). Mean χ values were calculated in five deep grey matter regions of interest (ROIs) provided with the phantom. Susceptibility maps were compared using the root mean squared error (RMSE) relative to the ground truth susceptibility map and the QSM-tuned structural similarity index (XSIM)[11].

In Vivo:

3D gradient-echo brain images of a healthy volunteer were acquired on a 3T Siemens Prisma MR system (National Hospital for Neurology and Neurosurgery, London, UK) using a 64-channel head coil. The image volume was tilted about the *x*-axis from -20° to +20° in 5° increments and acquired in 3 min 23 s (per volume) with TE1/ΔTE/TE5 = 4.92/4.92/24.60ms; TR=30ms; 1.23 mm isotropic voxels; 6/8 partial Fourier; and $GRAPPA_{PE}$ acceleration = 3.

For all angles/volumes, a total field map and noise map were obtained using a non-linear fit of the complex data[3]. A brain mask was created using BET[12,13], eroded by 6 voxels, and multiplied with a mask created by thresholding the inverse noise map at its mean to remove noisy voxels. Residual phase wraps were removed using Laplacian unwrapping[13,14] and background fields were removed using the Laplacian boundary value (LBV)[13,15] technique as it is independent of tilt angle. The four tilt correction schemes were compared using the same three χ calculation methods as for the numerical phantom.

For each angle, the magnitude image (RMS across echoes) was rigidly registered to the reference (0°) using NiftyReg[16] and the transformation matrix was used to transform the χ maps into the reference space for comparison. ROIs were obtained by registering the EVE[17] magnitude image with the same reference image and applying the resulting transformation to the EVE ROIs. Mean χ values were calculated in these ROIs for all angles. RMSE and XSIM were also used to compare tilt-corrected maps with the 0° reference susceptibility map.

Results

Numerical Phantom:

All QSM methods are most accurate with *RotPrior*, and least accurate with NoRot when the dipole is misaligned to the main magnetic field (Figure 2). wlTV is relatively robust to oblique acquisition, with *RotPrior* and *DipK* performing similarly. However, *DipK* shows variability in χ across angles in different ROIs. χ maps (Figure 3) make clearly apparent the errors resulting from *NoRot*.

In Vivo:

Figure 4 confirms that *NoRot* results in large susceptibility errors and that *RotPrior* is comparable to *DipK* between $\pm$20°, both performing better

than *DipIm*, in agreement with the phantom results. Difference images also confirm the phantom results (Figure 5). Subtle effects found in the phantom ROIs (Figure 2) were not apparent *in vivo* (not shown) due to noise, motion, rotation/registration interpolation effects and the expected variability in QSMs over repeated acquisitions[18].

Conclusions

We have shown that, for any susceptibility calculation method (TKD, iterative Tikhonov and wlTV) applied to an oblique acquisition, leaving the dipole kernel misaligned with the main magnetic field ($\hat{\mathbf{B}}_0$) direction, which is often the default mode of QSM toolboxes, leads to substantial χ errors. The most accurate susceptibilities can be obtained when local field maps are rotated into alignment with the scanner axes prior to χ calculation (*RotPrior*). For wlTV, accurate susceptibility calculation can be carried out in the tilted image frame without any rotations provided the correct ($\hat{\mathbf{B}}_0$) direction is used in defining the *k*-space dipole (*DipK*).

Acknowledgements

Oliver Kiersnowski is supported by the EPSRC-funded UCL Centre for Doctoral Training in Intelligent, Integrated Imaging in Healthcare (i4health) (EP/S021930/1). Karin Shmueli is supported by ERC Consolidator Grant DiSCo MRI SFN 770939. We thank Dr Carlos Milovic for his assistance with FANSI.

References

1. Dixon EC. Applications of MRI Magnetic Susceptibility Mapping in PET-MRI Brain Studies. Dr thesis, UCL (University Coll London). 2018. http://discovery.ucl.ac.uk/10053515/.
2. Marques, José P., et al. "QSM Reconstruction Challenge 2.0 Part 1: A Realistic in silico Head Phantom for MRI data simulation and evaluation of susceptibility mapping procedures." bioRxiv (2020).
3. Liu T, Wisnieff C, Lou M, Chen W, Spincemaille P, Wang Y. Nonlinear formulation of the magnetic field to source relationship for robust quantitative susceptibility mapping. Magn Reson Med. 2013 Feb;69(2):467-76. doi: 10.1002/mrm.24272. Epub 2012 Apr 9. PMID: 22488774.
4. Jenkinson M, Beckmann CF, Behrens TEJ, Woolrich MW, Smith SM. FSL. Neuroimage. 2012;62:782-790. doi:10.1016/j.neuroimage.2011.09.015
5. Shmueli K, De Zwart JA, Van Gelderen P, Li TQ, Dodd SJ, Duyn JH. Magnetic susceptibility mapping of brain tissue in vivo using MRI phase data. Magn Reson Med. 2009;62(6):1510-1522. doi:10.1002/mrm.22135
6. Karsa, A, Punwani, S, Shmueli, K, et al. An optimized and highly repeatable MRI acquisition and processing pipeline for quantitative susceptibility mapping in the head-and-neck region. Magn Reson Med. 2020; 84: 3206– 3222. https://doi.org/10.1002/mrm.28377
7. PMID: 32621302.MRI susceptibility calculation methods. https://xip.uclb.com/i/software/mri_qsm_tkd.html.
8. Schweser F, Deistung A, Sommer K, Reichenbach JR. Toward online reconstruction of quantitative susceptibility maps: Superfast dipole inversion. Magn Reson Med. 2013;69(6):1581-1593. doi:10.1002/mrm.24405
9. Bilgic B., Chatnuntawech I., Langkammer C., Setsompop K.; Sparse Methods for Quantitative Susceptibility Mapping; Wavelets and Sparsity XVI, SPIE 2015
10. Milovic C, Bilgic B, Zhao B, Acosta-Cabronero J, Tejos C. Fast Nonlinear Susceptibility Inversion with Variational Regularization. Magn Reson Med. Accepted Dec. 12th 2017. DOI: 10.1002/mrm.27073
11. Milovic C, Tejos C, and Irarrazaval P. Structural Similarity Index Metric setup for QSM applications (XSIM). 5th International Workshop on MRI Phase Contrast & Quantitative Susceptibility Mapping, Seoul, Korea, 2019.
12. S.M. Smith. Fast robust automated brain extraction. Human Brain Mapping, 17(3):143-155, November 2002.
13. http://pre.weill.cornell.edu/mri/pages/qsm.html

14. Schofield, Marvin A., and Yimei Zhu, 'Fast Phase Unwrapping Algorithm for Interferometric Applications', Optics Letters, 2003 https://doi.org/10.1364/ol.28.001194
15. Zhou, Dong, Tian Liu, Pascal Spincemaille, and Yi Wang, 'Background Field Removal by Solving the Laplacian Boundary Value Problem', NMR in Biomedicine, 27.3 (2014), 312–19 <https://doi.org/10.1002/nbm.3064>
16. Modat, et al. (2014). Global image registration using a symmetric block-matching approach. Journal of Medical Imaging, 1(2), 024003–024003. doi:10.1117/1.JMI.1.2.024003
17. Lim IA, Faria AV, Li X, Hsu JT, Airan RD, Mori S, van Zijl PC. Human brain atlas for automated region of interest selection in quantitative susceptibility mapping: application to determine iron content in deep gray matter structures. Neuroimage. 2013 Nov 15;82:449-69. doi: 10.1016/j.neuroimage.2013.05.127. Epub 2013 Jun 12. PMID: 23769915; PMCID: PMC3966481.
18. Xiang Feng, Andreas Deistung, Jürgen R. Reichenbach,Quantitative susceptibility mapping (QSM) and R2* in the human brain at 3T: Evaluation of intra-scanner repeatability, Zeitschrift für Medizinische Physik, Volume 28, Issue 1, 2018, Pages 36-48

Figures

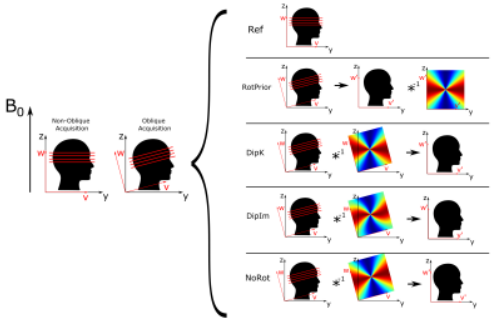

Figure 1: Schematic illustration of oblique acquisition and proposed tilt correction methods for QSM. The scanner frame (**x**,**y**,**z**) and the image frame (**u**,**v**,**w**) are shown with respect to the main magnetic field $\mathbf{B}_0=B_0\mathbf{z}$ (left). Proposed tilt correction methods are shown with the k-space dipole (right). *RotPrior* involves rotation of the tilted image frame into alignment (**u'**,**v'**,**w'**) with the scanner frame. *NoRot* represents incorrectly misaligning the dipole kernel with $B_0\mathbf{z}$ simulating a common error.

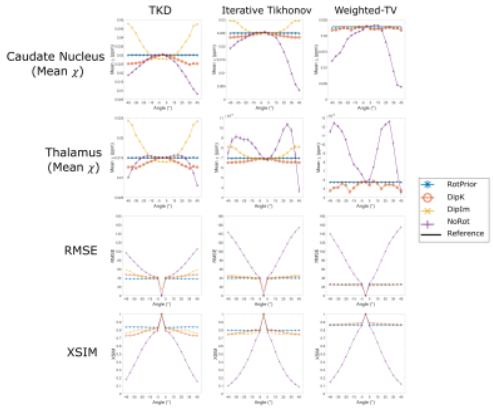

Figure 2: Mean susceptibilities in the Caudate and Thalamus (top rows), and RMSE and XSIM (bottom rows) across all tilt angles for all tilt correction schemes and all three calculation methods in the numerical phantom. *NoRot* performs worst across all angles. *RotPrior* is the most accurate tilt correction scheme. For weighted linear TV, *DipK* and *RotPrior* have similar XSIM values but the mean thalamus varies more over angles with *DipK*. Note that *DipIm* is not shown for wlTV as this method fails.

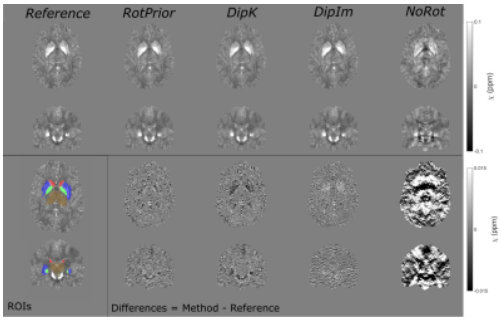

Figure 3: χ maps and difference images illustrating the effects of all tilt correction schemes in the numerical phantom. An axial and a coronal slice are shown for a volume tilted at 25° and a reference 0° volume with all χ maps calculated using the iterative Tikhonov method. The ROIs analysed are also shown (bottom left). Qualitatively, *RotPrior* performs the best while *NoRot* results in substantial χ errors across the whole brain. The results from TKD and weighted linear TV (not shown) are very similar.

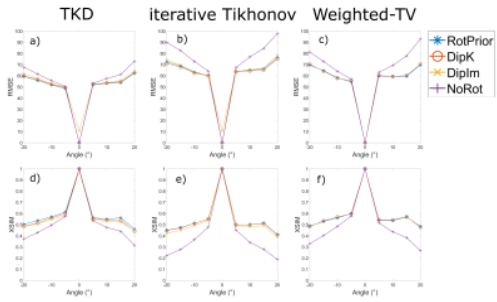

Figure 4: RMSE and XSIM plots over all angles for all tilt correction schemes and all three χ calculation methods in one subject *in vivo*. These results are similar to those in the numerical phantom (Figure 2) with *RotPrior* and *DipK* performing best and *NoRot* performing worst across all methods. At non-zero tilt angles, RMSE and XSIM have a respectively high/low baseline level arising from rotation and registration interpolations. *DipIm* fails for wlTV and is, therefore, omitted from the plots in the last column.

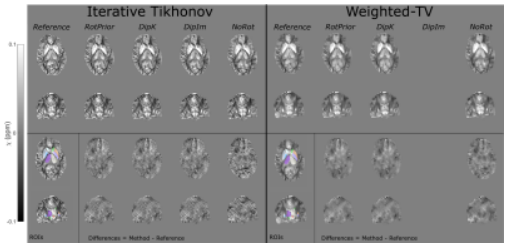

Figure 5: χ maps and difference images illustrating the effects of all tilt correction schemes *in vivo*. An axial and a coronal slice are shown for a volume tilted at -10° and a reference (0°) volume with all χ maps calculated using the iterative Tikhonov method (left) and weighted linear TV (right). *NoRot* leads to the largest differences and image artefacts throughout the brain. The EVE ROIs used are shown (bottom left). Results from TKD (not shown) are very similar.

Proc. Intl. Soc. Mag. Reson. Med. 29 (2021)
0794